The Cryosphere, 10, 385–399, 2016
www.the-cryosphere.net/10/385/2016/
doi:10.5194/tc-10-385-2016

The Cryosphere Open Access EGU

Tremor during ice-stream stick slip

B. P. Lipovsky[1] **and E. M. Dunham**[1,2]

[1]Department of Geophysics, Stanford University, Stanford, CA, USA
[2]Institute for Computational and Mathematical Engineering, Stanford University, Stanford, CA, USA

Correspondence to: B. P. Lipovsky (lipovsky@stanford.edu)

Received: 1 September 2015 – Published in The Cryosphere Discuss.: 30 September 2015
Revised: 24 December 2015 – Accepted: 14 January 2016 – Published: 16 February 2016

Abstract. During the 200 km-scale stick slip of the Whillans Ice Plain (WIP), West Antarctica, seismic tremor episodes occur at the ice–bed interface. We interpret these tremor episodes as swarms of small repeating earthquakes. The earthquakes are evenly spaced in time, and this even spacing gives rise to spectral peaks at integer multiples of the recurrence frequency ∼10–20 Hz. We conduct numerical simulations of the tremor episodes that include the balance of forces acting on the fault, the evolution of rate- and state-dependent fault friction, and wave propagation from the fault patch to a seismometer located on the ice. The ice slides as an elastic block loaded by the push of the upstream ice, and so the simulated basal fault patch experiences a loading velocity equal to the velocity observed by GPS receivers on the surface of the WIP. By matching synthetic seismograms to observed seismograms, we infer fault patch area ∼10 m^2, bed shear modulus ∼20 MPa, effective pressure ∼10 kPa, and frictional state evolution distance ∼1 μm. Large-scale slip events often occur twice daily, although skipped events have been increasing in frequency over the last decade. The amplitude of tremor (recorded by seismometers on the ice surface) is greater during the double wait time events that follow skipped events. The physical mechanism responsible for these elevated amplitudes may provide a window into near-future subglacial conditions and the processes that occur during ice-stream stagnation.

1 Introduction

Concern about future sea level rise motivates a study of the subglacial conditions that give rise to streaming ice (Joughin and Alley, 2011). The Whillans Ice Plain (WIP) region of the West Antarctic Ice Sheet (WAIS) is notable for decelerating from previously fast streaming flow over the instrumental record (Beem et al., 2014). Since most ice flux in Antarctica occurs through ice streams (Whillans et al., 1987; Rignot et al., 2011), understanding the conditions that cause ice-stream stagnation is of basic importance in constraining the continent's contribution to future sea level rise. Although recent progress has been made in describing the relationship between basal conditions and ice stream motion (Bougamont et al., 2011, 2015; Robel et al., 2013; Kyrke-Smith et al., 2014, 2015), direct observation of the temporal variation in subglacial conditions during ice-stream stagnation has remained elusive.

Antarctic ice streams exhibit a wide variety of stick-slip behavior. The WIP is an extreme case wherein the entire $\sim 2\times10^4$ km^2 ice plain undergoes tidally modulated once- or twice-daily stick-slip motions (Bindschadler et al., 2003; Wiens et al., 2008). During the time between large-scale sliding events, several ∼100 km^2 regions exhibit a high degree of locking (Winberry et al., 2014c). Slip motion observed by on-ice GPS instruments (Fig. 1) then begins within the locked region and propagates outward towards the ice stream margins and grounding zone (Pratt et al., 2014).

The focus of our study is a type of seismic tremor first identified by Winberry et al. (2013) that occurs during large-scale slip motion. We follow Winberry et al. (2013) in attributing these tremor episodes to small repeating earthquakes at the bed of the WIP (Fig. 2 and Sect. 3). The earthquakes are evenly spaced in time, and this even spacing gives rise to spectral peaks that are inversely proportional to the earthquake recurrence time (Fig. 3d) (Powell and Neuberg, 2003; MacAyeal et al., 2008). Over the 30 min duration of a tremor episode, the earthquake recurrence time gradually changes, causing the spectral peaks to glide (Fig. 3a).

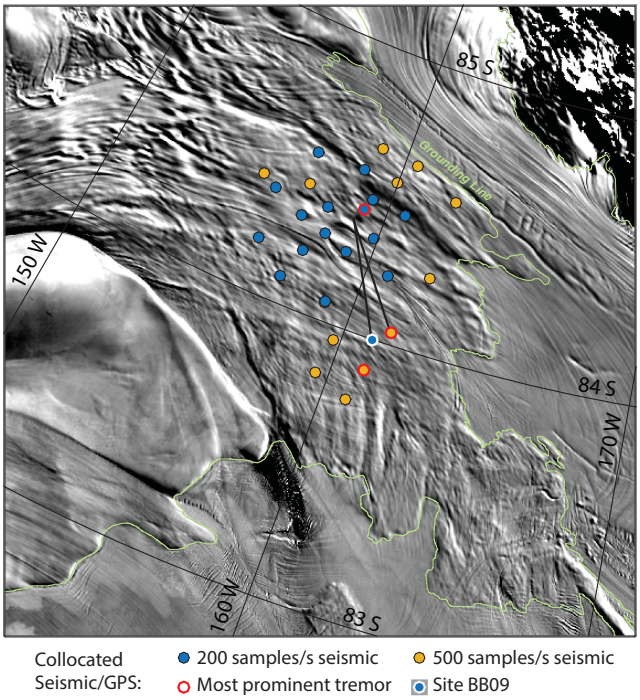

Figure 1. Map of the Whillans Ice Plain (WIP) and surrounding area. The dots show the collocated seismometer-GPS deployments used in this study. The yellow dots indicate the locations of seismometers recording at 500 Hz, the blue dots indicate the locations of seismometers recording at 200 Hz, the white outline around a dot shows the location of the station BB09, and the red outline shows the location of the seismometers that most clearly record the tremor signal. The grounding line is shown in green. The grayscale background is from the MODIS composite image of Antarctica (Scambos et al., 2007; Haran et al., 2014).

The goal of this study is to quantitatively describe the relationship between conditions at the bed of WIP and the tremor that occurs there. To do this, we simulate the evolution of elastic and frictional forces along a small fault patch at the boundary between the ice and bed (Sect. 5). Rapid motion along the fault excites waves that are recorded at a seismometer, and we account for this wave propagation to place constraints on the source properties by matching the amplitude and other features of the tremor signals. The simulated tremor-producing fault patch is loaded with surface velocity data recorded using GPS stations on the WIP.

A basic question is whether the events occur at an ice–ice, ice–till, or ice–bedrock interface. An observation of fundamental importance in this regard is that observed seismic particle velocity amplitudes are $\sim$100 nm s^{-1}, which is quite low given the source–station distance even for tremor patch sizes $\sim$1 m. Low seismic amplitudes could exist for a number of reasons such as low stress drop and hence slip. However, we are able to constrain slip independently without using the amplitude. We instead find that the effect of slip along a bi-material interface is of leading importance. Specifically, when seismic slip occurs at an interface between a rigid and a compliant material, more motion occurs in the compliant material. All else being equal, lower seismic amplitudes therefore constitute evidence for a highly compliant bed material.

We also report a previously undocumented phenomenon: tremor amplitudes are anomalously high during large-scale slip events that follow a skipped slip event. In Sect. 7, we propose two distinct mechanisms to account for the observed anomalous seismic amplitudes: stiffening of the bed and reduction of aseismic slip. Skipped events have become more frequent in the last decade (Winberry et al., 2014c). The physical conditions that result in elevated seismic amplitudes during tremor may therefore be related to the conditions that will prevail in the near-future if stagnation continues.

2 Observations

We examine collocated seismic and geodetic data collected at the WIP during field seasons in 2010–2011 and 2011–2012 (Fig. 1) (Winberry et al., 2014a, b). The data show large-scale sliding events, wherein the ice surface velocity accelerates to an elevated value and then gradually decays over a period of about 15 min. Several GPS time series are plotted in Fig. 4c. In this figure, the data are aligned so that $t = 0$ corresponds to the time of maximum sliding velocity for each event. GPS data are recorded at 15 samples s^{-1}. The fastest recorded velocity observed during any of the sliding events in our data set is 7.47×10^{-4} m s^{-1} or 64.5 m d^{-1}. We low pass filter all GPS data below 500 s.

Large-scale sliding events are observed either one or two times per day. Ocean tides in the Ross sea feature a strong diurnal component, and the timing of slip events is nearly synchronous with the high and low ocean tides (Bindschadler et al., 2003). Skipped events are usually low tide events, with the subsequent slip event occurring at high tide. The event flowing a skipped event is termed a double wait time event, and double wait time events have unique properties that we describe in Sect. 7.

During large-scale sliding events, seismometers record tremor episodes that consist of repeating velocity pulses (Fig. 3c). The spacing between the pulses changes from being as fast as 30 pulse s^{-1} to as slow as about 1 pulse s^{-1}. The pulse rate is approximately proportional to the ice surface velocity during a large scale slip event, suggesting that the overall ice motion is somehow driving the tremor. Additionally, at some stations the pulse rate is sufficiently low ($\lesssim$1 Hz) that seismograms show individual P- and S-waves (Winberry et al., 2013).

A remarkable feature of the observed seismograms is seen in spectrograms as the smooth variation, or gliding, of the spectral peaks during the duration of large-scale sliding (Fig. 3a). The lowest frequency spectral peak occurs at the inverse of the pulse rate. This fundamental frequency $f_0(t)$ is accompanied by overtones that are present at integer mul-

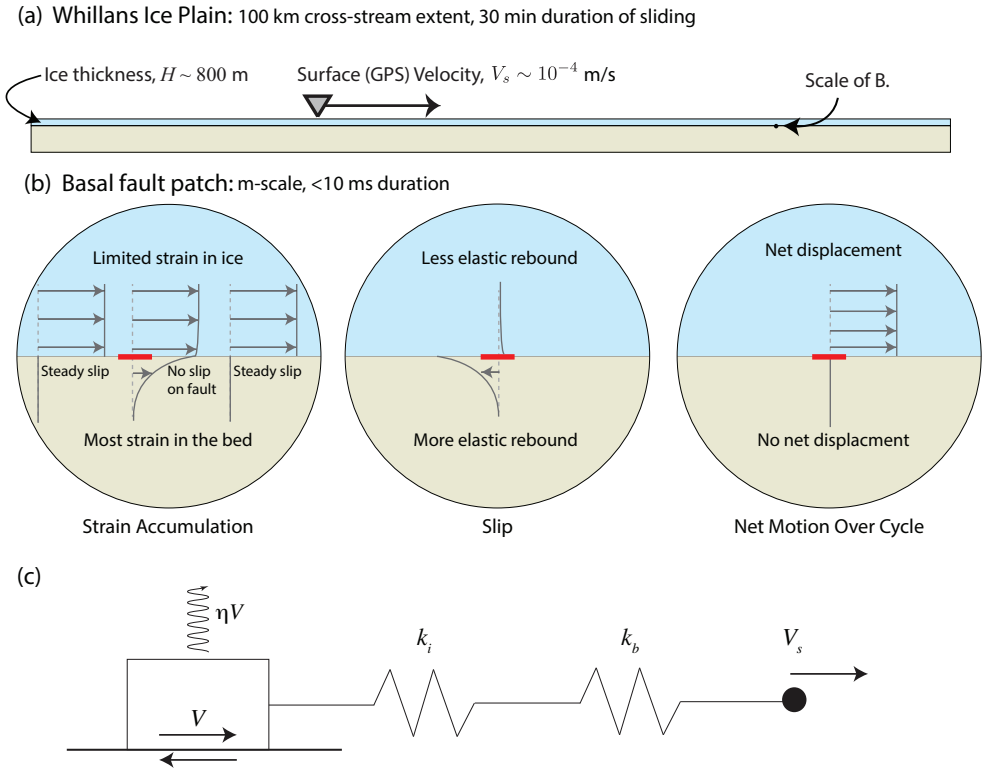

Figure 2. Schematic illustration showing the spatial and temporal scales of stick-slip motion in the Whillans Ice Plain (WIP). **(a)** The entirety of the WIP undergoes stick-slip motion with 100 km extent. During this time, the ice slides with elevated velocity for approximately 30 min duration. **(b)** During large-scale sliding, small repeating earthquakes happen with duration less than 10 ms on fault patches with radius ~ 1 m. The tremor-producing patch is shown as a red bar, and the arrows represent particle displacements. Through our analysis we infer a compliant bed which implies that more motion occurs in the till than in the ice at the scale of the tremor patch. **(c)** Diagram of a mechanically analogous system showing the load point velocity, two springs in series, a frictional element, and the damping effect of radiated seismic waves. The ice and bed stiffnesses, k_i and k_b, are discussed in Sect. 5.1.

tiples, i.e., $2f_0, 3f_0$, and so on. We implement a basic feature tracking algorithm to calculate $f_0(t)$ from spectrograms of several tremor episodes, and the result is shown in Fig. 4b.

Tremor episodes occur during all large-scale sliding events cataloged by Pratt et al. (2014) for which seismic data are available, and tremor episodes have never been observed when large-scale sliding is not occurring. Several stations have clearly visible tremor episodes. Every station for which data are available as of December 2015, however, shows at least a brief period during which some features of tremor episodes are present. The tremor episodes are most clearly observed when more than three spectral peaks are present. Clearly observed tremor is most common at the stations BB09 and GS17, although stations BB02 and GS07 near BB09 also have multiple tremor bands. These three stations are located in regions of the WIP, where more than 90 % of sliding occurs during large-scale slip events (Winberry et al., 2014c, their Fig. 3a), although not all stations located in such regions exhibit equally clear tremor. We primarily focus on data from BB09. When GPS data are not available for this station, we combine GPS data from BB02 with seismic data from BB09. These stations are located 6 km apart, and for an average rupture velocity on the order of 100–300 m s^{-1} (Walter et al., 2011, 2015), the resulting 20–60 s delay is small compared to the $\sim$1800 s duration of large-scale slip.

Tremor episodes have peak seismic amplitudes on the order of 400–700 nm s^{-1}. An important terminology note is that we distinguish between high frequency particle velocity amplitudes v ("seismic amplitudes") recorded using seismometers and ice surface velocities V_s recorded using GPS instruments. Quantifying the variation of seismic amplitudes with time is challenging because the data are noisy and broadband (Trigg, 2006, p. 99). We calculate the seismic particle velocity amplitude envelope using the following algorithm. We first make a vector of all peaks in the time series. We then calculate a second vector by applying the peak finder to this vector of peaks. This process is carried out repeatedly until the spacing between peaks approaches $\sim$10 s. The result seismic particle velocity amplitudes are shown for several tremor episodes in Fig. 4a. To verify that this measure of seismic amplitude has no obvious pathological behavior, we compare it to another amplitude metric in Sect. 7.

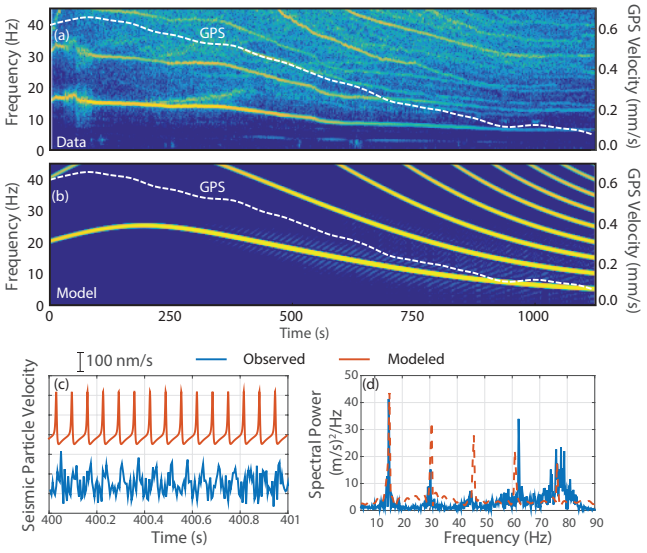

Figure 3. Comparison between observed **(a)** and modeled **(b)** tremor episode spectrograms for the episode that occurred on 14 January 2011 at 11:31. The white dashed line is the observed GPS velocity. The logarithmic color scales in both spectrograms are the same and have units of power spectral amplitude $(\mathrm{m\,s^{-1}})^2$ / Hz. The data were high-pass filtered above 1 Hz before creating the spectrograms. The spectrograms use an 800 sample window with 50 % overlap. We compare the modeled (red) and observed (blue) seismic velocity trace in **(c)** and frequency spectrum in **(d)**. The frequency spectrum in **(d)** is calculated over four second time windows for both the data and the model. Spectral bands from other, lower amplitude tremor sources are also present in the data shown in **(a)**.

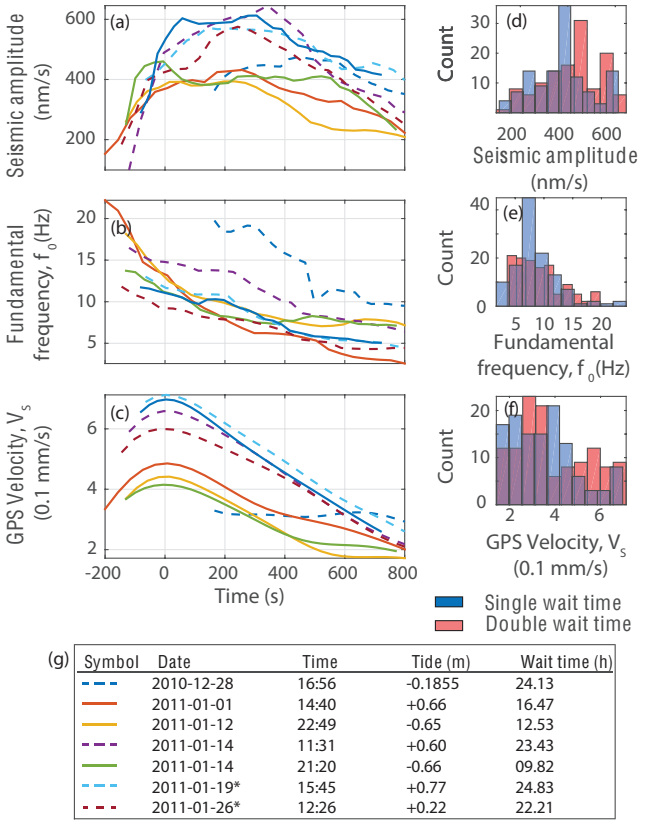

(g)

Symbol	Date	Time	Tide (m)	Wait time (h)
	2010-12-28	16:56	-0.1855	24.13
	2011-01-01	14:40	+0.66	16.47
	2011-01-12	22:49	-0.65	12.53
	2011-01-14	11:31	+0.60	23.43
	2011-01-14	21:20	-0.66	09.82
	2011-01-19*	15:45	+0.77	24.83
	2011-01-26*	12:26	+0.22	22.21

Figure 4. Time series **(a–c)** and histograms **(d–f)** of observed parameters for six tremor episodes. Events with wait times greater than 17 h (double wait time events) are shown with dashed lines and events with wait times less than 17 h (single wait time events) are shown with solid lines. Collocated GPS data were not available at BB09 for the events marked with asterisks; data were used from the station BB02 for these events.

The repeating velocity pulses each have duration on the order of 1/40 to 1/80 s. Pulse durations were mildly undersampled during the 2010–2011 field season when the sampling rate was 200 samples $\mathrm{s^{-1}}$. During the 2011–2012 field season, data were recorded at 500 samples $\mathrm{s^{-1}}$; we refer to these latter data as the "high rate" data. To quantify the effects of undersampling, we examine 25 tremor episodes recorded at high rate at 10 different seismometers. We observe no pulse duration less than 1/100 s. Extrapolating this finding to the data recorded at low rate suggests that we may interpret the pulse duration recorded at low-rate seismometers, even if it is only recorded over 3–6 data points. Undersampling may additionally result in amplitude reduction. We find that over the tremor episodes that we examine from the second field season, the amplitude reduction that occurs by low pass filtering data below 100 Hz is $12.5\,\% \pm 0.5\,\%$. We therefore correct the undersampled data from the first field season by scaling their amplitudes by a factor of 1.125.

We find that tremor episodes during double wait time events have higher seismic amplitudes than tremor episodes during single wait time events. Although large scale motion of the WIP has been shown to have higher sliding velocity during double wait time events (Walter et al., 2015), to our knowledge, such an association has not previously been noted for tremor amplitudes. We quantify some implications of this finding in Sect. 7.

3 Motion at the tremor-producing patch

We interpret each individual velocity pulse during a tremor episode as the far field expression of motion on a small fault patch. We refer to this patch as the tremor producing patch. Tremor episodes are interpreted as families or swarms of repeating earthquakes where the observed pulse rate is the earthquake recurrence rate.

At least two observations support this interpretation. First, small repeating earthquakes are expected to repeat with a faster recurrence rate at higher loading velocities, and this is observed in the data from the WIP. Second, at low pulse rate, Winberry et al. (2013) noted the presence of individually discernible events with clear P- and S-wave arrivals. This observation implies that tremor is composed of many rapidly

repeating events rather than resonance of a fluid-filled crack of cavity (Lipovsky and Dunham, 2015) or wave propagation effects (Bean et al., 2014; Lough et al., 2015).

Motion of the WIP is due to the longitudinal stresses that result from the push of upstream ice. This loading occurs within the ice column, which results in a net motion of the ice during large-scale slip events. We assume that the ice and the bed deform elastically, a valid approximation over the 15 min duration of a tremor episode (Fig. 2) (Goldberg et al., 2014). Throughout the earthquake cycle on the tremor patch, most motion occurs on the side of the patch that has the more compliant material (Fig. 2b, center). We discuss elastic strain partitioning between the ice and the bed in greater detail in Sect. 5.1.

Slip $\delta(\boldsymbol{x},t)$ at a point $\boldsymbol{x}$ on the ice–bed interface is defined as the difference in displacement between the upper and lower faces of the interface. The portion of the ice–bed interface outside the tremor-producing patch experiences relatively steady slip at nearly constant shear stress. This shear stress holds the bed in an elastically deformed state but causes no accelerations there. For this reason, outside the tremor-producing patch the slip rate $V(\boldsymbol{x},t) = \partial\delta(\boldsymbol{x},t)/\partial t$ is equal to the surface velocity V_s. When the tremor-producing patch is locked it experiences no slip and strain accumulates in time at a rate proportional to V_s (Fig. 2b, left) and inversely proportional to the patch size. Accompanying this straining is an increase in stress on the patch, which ultimately fails in a small slip event than relaxes the stress.

The tremor-producing patch thus experiences variations in the basal shear stress that give rise to stick-slip oscillations (Sect. 5). In this study we do not attempt to resolve the spatial details of the slip process, given that seismic wavelengths in the available data are larger than the patch size. We therefore focus on the spatially averaged slip,

$$D(t) = \frac{1}{A}\int_{\substack{\text{tremor patch}\\ \text{surface}}} \delta(\boldsymbol{x},t)\,\mathrm{d}A$$

$$= \frac{1}{A}\int_{t_0}^{t}\int_{\substack{\text{tremor patch}\\ \text{surface}}} V(\boldsymbol{x},t')\,\mathrm{d}A\,\mathrm{d}t', \qquad (1)$$

where t_0 is the time at the beginning of a tremor slip event. The total slip in one event is achieved after a duration of $T \sim 1/80$ s. Whereas $D(t)$ refers to the cumulative spatially averaged slip, we use the notation D (without an explicit argument) to refer to the spatially averaged total slip in a single event.

The sliding velocity of the tremor-producing patch averaged over many slip cycles is approximately $D f_0$ for slip pulses that are evenly separated in time by f_0^{-1}. This relationship assumes that all motion occurs during seismically

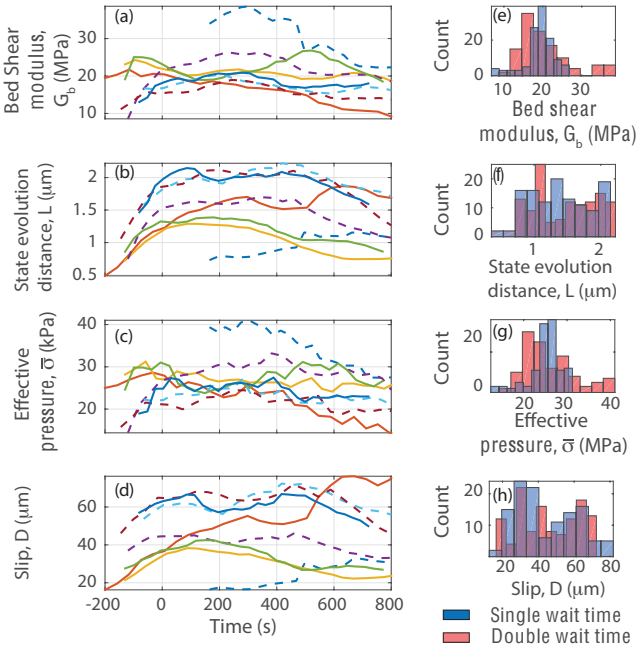

Figure 5. Time series of inferred parameters **(a–d)** and their histograms **(e–h)** for six tremor episodes. Properties of the events are listed in the table in Fig. 4g. The colors and symbols used in the time series and histograms are the same as in Fig. 4.

expressed slip events, as we discuss in greater length in Sect. 7.2. Over multiple earthquake cycles the sliding velocity must keep pace with the surface velocity of the ice V_s,

$$D = V_\mathrm{s} / f_0. \qquad (2)$$

Using observations of V_s and f_0, we infer values of $D \approx 15$–$75\,\mu$m (Fig. 5d). Seismograms sometimes show multiple tremor episodes that are simultaneously recorded at a single station. In Fig. 3a, for example, these tremor bands appear as low as 1–2 Hz. These tremor events have D as large as 1 mm.

4 Wave propagation

We now describe the relationship between slip on the tremor-producing patch and the seismic particle velocity amplitudes recorded at on-ice seismometers. In our description, these amplitudes are influenced only by the accelerations on the tremor patch, tremor patch size, geometrical spreading, and potential bi-material effects arising from the fault being located at the interface between ice and the bed material. Attenuation is thought to be unimportant at the frequencies of interest in the present study based on the following reasoning.

The seismic quality factor Q for ice is in the range 400–1000 over all of Antarctica (Peters et al., 2012). For wave propagation distances on the order of the ice thickness H, attenuation becomes important only at frequencies greater than

a characteristic attenuation frequency

$$f_* \equiv Q c_\mathrm{i} / \pi H. \tag{3}$$

The shear wave speed of ice is denoted c_i. At 250 Hz, the highest Nyquist frequency in our data set, attenuation would become important if $Q < 315$. We therefore do not expect attenuation to be important for the frequencies that are resolved in our data set.

Far field seismic particle velocity due to fault motion in a uniform medium is given by (Aki and Richards, 2002, Eq. 4.96),

$$v(t) = \frac{\ddot{M}(t - H/c_\mathrm{i})}{4\pi \rho_\mathrm{i} c_\mathrm{i}^3 H}, \tag{4}$$

where the seismic moment is defined as

$$M(t) \equiv \pi G_\mathrm{i} R^2 D(t), \tag{5}$$

for a circular fault patch with radius R and ice shear modulus G_i. Here, and in later expressions, the overdot denotes $\partial / \partial t$. This expression for particle velocity is specific to far field S waves that propagate from the source to the station through a lobe in the far field S-wave radiation pattern. This is consistent with horizontal faults located directly below the stations. If the station is not directly over the source, or the fault has different orientation, then the station will record both P and S waves; the expression for far field P waves has the same form, but with c_i replaced by the ice P-wave speed. Thus, by assuming stations directly over the source, we are taking the smallest possible value of epicentral distance times wave speed cubed in the denominator, which will maximize particle velocity for a given seismic moment.

Despite this sensitivity to wave type and radiation pattern, we do not attempt to model distinct P- and S-waves because they are not clearly present in the data during tremor events. When single basal events do show clear P- and S-wave arrivals, their relative timing suggests a hypocentral distance of about one ice thickness (Winberry et al., 2013). For this reason, we take the hypocentral distance to be equal to the ice thickness for the remainder of this work, but with an awareness of how this assumption might bias our estimates of source parameters.

The far field seismic velocity field predicted by Eq. (4) does not account for the contrast in material properties in the vicinity of the bed (Table 1). We consider two variations of Eq. (4) that account for material property heterogeneity. The first type of heterogeneity that we consider is that where the region surrounding the fault and the region surrounding the seismometer are both homogeneous but have different material properties. The far field seismic velocity is (Anandakrishnan and Bentley, 1993; Aki and Richards, 2002),

$$v(t) = \frac{\ddot{M}(t - H/c_\mathrm{i})}{2\pi \sqrt{z_\mathrm{i} z_\mathrm{b}} c_\mathrm{i}^2 H}, \tag{6}$$

where the shear wave impedances are denoted $z_k = \rho_k c_k$ (no summation) and z_i and z_b are the shear wave impedances of the ice and bed. The amplitudes predicted by Eq. (6) are valid for media with gradually varying material properties and may therefore be relevant to some aspects of ice sheet seismology (Wittlinger and Farra, 2012). The relationship Eq. (6), however, cannot account for the sharp changes in material properties that are expected to occur at the ice–bed interface.

The second type of heterogeneity that we consider is that where the fault patch is located at the ice–bed interface. A rich variety of wave behavior occurs when slip occurs along a fault that separates media with different elastic properties (Ben-Zion, 1990). We neglect head wave phases whose ray path partially travels along the bed. We take the short-time limit of Eq. (26) of Ben-Zion (1990) and find that the far field particle velocity amplitudes are sensitive to the material properties on both sides of the fault through the impedance parameter Z,

$$Z = \frac{z_\mathrm{b}}{z_\mathrm{i} + z_\mathrm{b}}. \tag{7}$$

Seismic moment Eq. (5) is not well defined for slip on a bi-material interface (Ampuero and Dahlen, 2005), in which case a more useful quantity is seismic potency,

$$P(t) \equiv \pi R^2 D(t). \tag{8}$$

Far-field seismic particle velocity amplitudes are given by

$$v(t) = Z \frac{\ddot{P}(t - H/c_\mathrm{i})}{\pi c_\mathrm{i} H}. \tag{9}$$

We have invoked a factor of 2 higher amplitudes to account for amplification at the free surface (p. 130 in Aki and Richards, 2002).

We find a scaling relationship for the far field particle velocity Eq. (9) by replacing time derivatives with the event duration T:

$$v \sim Z \frac{D}{c_\mathrm{i} H} \left(\frac{R}{T} \right)^2. \tag{10}$$

The factor of R/T has the interpretation of a rupture velocity, and it is interesting to note that for fixed material properties, seismic amplitudes depend only on slip and rupture velocity.

5 Forces acting on the fault patch

5.1 The elastic response

We now examine the forces acting on the tremor-producing patch. We first calculate the patch stiffness k for a circular fault patch of radius R on a bi-material interface. The patch stiffness relates slip on the patch D to the static stress drop $\Delta\tau$:

$$\Delta\tau = kD \equiv \frac{G_*}{R} D. \tag{11}$$

Table 1. Table of material properties that are held fixed.

Quantity	Symbol	Unit	Value
Ice shear modulus	G_i	MPa	3664
Ice density	ρ_i	$\mathrm{kg\,m^{-3}}$	916
Ice Poisson ratio	ν_i		0.33
Ice quality factor	Q		750
Ice wave speed	c_i	$\mathrm{m\,s^{-1}}$	2000
Ice thickness	H	m	800 m
Bed density	ρ_b	$\mathrm{kg\,m^{-3}}$	1700
Bed Poisson ratio	ν_i		0.49
Nominal friction coefficient	μ_0		0.4
Nominal sliding velocity	V_0	$\mathrm{m\,s^{-1}}$	10^{-5}
State evolution distance	L	m	10^{-6}
Direct effect parameter	a		5×10^{-3}
Healing parameter	b		15×10^{-3}
Maximum observed sliding velocity	V_max	$\mathrm{m\,s^{-1}}$	7.47×10^{-4}

The modulus G_* is the effective shear modulus of the bimaterial interface. Both the patch stiffness k and the effective shear modulus G_* depend on the elastic constants on both sides of the sliding interface. The effective patch modulus is calculated by taking derivatives of the strain energy function of Willis (1972) as described by Aki and Richards (2002) in their Eq. (2.31). Two limiting cases are the case of identical materials and the case of dissimilar materials. When material properties on both sides of the fault patch are identical, $G_* = (32G/15\pi)$ for Poisson ratio $\nu = 1/3$ (Eshelby, 1957). When one material is much more rigid than the other, G_* becomes independent of the elastic properties of the more rigid material. If Poisson's ratio is chosen to represent ice ($\nu_\mathrm{i} = 1/3$) and till ($\nu_\mathrm{b} = 0.49$), the resulting effective patch shear modulus is $G_* \approx 3.5G_\mathrm{b}$.

Displacement occurs on both sides of the fault patch. The displacements of the two sides add together in series to give the total slip, $D = D_\mathrm{i} + D_\mathrm{b}$, where D_i is the displacement in the ice and D_b is the displacement in the bed. Then, in the spirit of (11), we may define the stiffnesses of the ice and bed as $k_\mathrm{i} \equiv \Delta\tau\,/\,D_\mathrm{i}$ and $k_\mathrm{b} \equiv \Delta\tau\,/\,D_\mathrm{b}$. The total stiffness is then given by $1\,/\,k = 1\,/\,k_\mathrm{b} + 1/k_\mathrm{i}$. This situation, which can be idealized in terms of a spring-slider system with two springs in parallel, is shown schematically in Fig. 2c. It is important to note that both stiffnesses are functions of the material properties on both sides of the interface.

The shear stress τ experienced by the small fault patch is

$$\frac{\mathrm{d}\tau}{\mathrm{d}t} = -k(V - V_s) - \eta\frac{\mathrm{d}V}{\mathrm{d}t}, \tag{12}$$

where V is the spatially averaged sliding velocity on the patch surface, t is time, and the radiation damping parameter is (Geubelle and Breitenfeld, 1997)

$$\eta \equiv \left(\frac{1}{z_\mathrm{i}} + \frac{1}{z_\mathrm{b}}\right)^{-1}. \tag{13}$$

The right-hand side of Eq. (12) represents the contribution to the shear stress rate due to elasticity. The first term is the static elastic stressing rate. Static elastic strains accumulate in the region surrounding the fault during the period between slip pulses. The static elastic stress term describes the contribution to the stressing rate from this loading. The second term is an approximate inertial stressing rate. In an instantaneous amount of time after slip initiates on the fault patch, shear waves emanate away from the patch and have a damping effect. The radiation damping term accounts for the stress change carried by these waves.

The duration of slip arises from a balance between these two terms and is given by

$$T \equiv \frac{\eta}{k} \sim \frac{R\eta}{G_*} \sim 1/f_\mathrm{c}, \tag{14}$$

where the corner frequency is denoted f_c. Equation (14) is a scaling law for the earthquake duration that arises from balancing the two terms on the right-hand side of Eq. (12). It is not an equality (Brune, 1970; Madariaga, 1976; Kaneko and Shearer, 2014) and actual earthquake durations vary for many reasons including variable rupture velocity and whether a rupture is bilateral or unilateral. We expect these additional features to introduce factors of order unity into Eq. (14). For the purposes of this study, we consider Eq. (14) to be adequate.

5.2 Friction

Elastic forces are balanced by friction. Frictional stresses change in time according to Rice et al. (2001)

$$\frac{\mathrm{d}\tau}{\mathrm{d}t} = \frac{a\bar{\sigma}}{V}\frac{\mathrm{d}V}{\mathrm{d}t} - \frac{V}{L}\left[\tau - \mu_\mathrm{ss}(V)\bar{\sigma}\right], \tag{15}$$

where $\bar{\sigma} = \sigma - p$ is the effective pressure due to normal stress σ and pore pressure p. The steady state coefficient of friction $\mu_\mathrm{ss}(V)$ is given by

$$\mu_{ss}(V) = \mu_0 - (b-a)\log(V/V_0). \quad (16)$$

The parameters μ_0, a, b, and V_0 are the nominal coefficient of friction, the direct effect parameter, the healing parameter, and the reference velocity. The first term on the right-hand side of Eq. (15) represents the laboratory-observed instantaneous increase of frictional resistance to sliding with an increase in sliding velocity. The magnitude of this so-called direct effect is characterized by the parameter a. The second term on the right-hand side of Eq. (15) represents the evolution of frictional resistance to a steady state value $\mu_{ss}(V)$ that depends on the sliding velocity. This evolution occurs over the state evolution distance L. Larger values of L correspond to systems that evolve to steady state after a greater amount of sliding. The change in steady frictional resistance to sliding Eq. (16) at two different sliding velocities is proportional to $(b-a)$ and to the logarithm of the ratio of the velocities.

The distinction between velocity-strengthening behavior at slip distances less than L (the direct effect) and velocity-weakening behavior at slip distance greater than L (the steady state response that follows state evolution) is of central importance in contemporary understanding of frictional stick-slip behavior. The direct effect is required for mathematical well-posedness of the sliding problem for steady state velocity-weakening friction (e.g., Rice et al., 2001). Another important consequence of this frictional description is the emergence of a minimum patch size or nucleation length that is required for unstable fault slips and earthquakes. This minimum patch size is controlled by the state evolution distance L, and for the frictional configuration considered in this study, is directly proportional to L.

The appropriateness in glaciology of a friction law of this type has been demonstrated by numerous studies (Thomason and Iverson, 2008; Rathbun et al., 2008; Iverson, 2010; Zoet et al., 2013). These studies examined the frictional properties of till-on-clast sliding (Thomason and Iverson, 2008), till-on-till sliding (Rathbun et al., 2008), and ice-on-rock sliding (Zoet et al., 2013). Each conducted velocity-step and slide–hold–slide experiments, Thomason and Iverson (2008) on a ring-shear device and Rathbun et al. (2008) and Zoet et al. (2013) in a biaxial shear apparatus. A description such as Eq. (15) may be thought of as a refinement to the generally accepted frictional-plastic rheological description of till (Tulaczyk et al., 2000) and as generalization of a frictional model consisting only of static and dynamic coefficients of friction (e.g., Sergienko et al., 2009).

5.3 Stability of steady sliding

The system of Eqs. (12), (15), and (16) is amenable to traditional linear stability analysis. One prediction of such an analysis is the condition under which the stick-slip instability occurs. This type of analysis was carried out by Dmitrieva et al. (2013) for perturbations about steady sliding at rate V_s. Dmitrieva et al. (2013) found that the transition between steady sliding and stick-slip motion occurs when (their supplemental equation (8)),

$$\frac{(b-a)\bar{\sigma}}{L} \geq k + \frac{\eta V_s}{L}. \quad (17)$$

Equality in Eq. (17) is achieved at neutral stability. Dependence on the patch size R enters Eq. (17) through the patch stiffness k. The left-hand side of Eq. (17) represents the variation in frictional strength per slip increment $d\tau_{str}/dD$. The right-hand side of Eq. (17) represents the variation in elastic stress per slip increment $d\tau_{el}/dD$.

The stability condition Eq. (17) has two dominant balances that result from balancing each of the elastic components on the right-hand side with the strength term on the left-hand side. The static stability limit occurs when $(b-a)\bar{\sigma}$ is balanced by kL. In this limit, the sliding is stabilized by the static elastic stiffness of the near-fault material. The inertial stability limit occurs when $(b-a)\bar{\sigma}$ is balanced by ηV. In this limit, sliding is stabilized by the damping effect of waves that are radiated during periods of higher sliding velocity.

5.4 Simulations of tremor events

We carry out simulations of a spring slider system that obeys the governing Eqs. (12), (15), and (16). We use observed surface velocity data recorded on the ice to load the fault in our simulations; i.e., the loading velocity is set equal to the observed surface velocity as measured by a GPS station deployed on the Whillans Ice Stream at station BB09. The GPS data are interpolated using a cubic spline. The system of equations is solved in MATLAB using the Runge–Kutta solver *ode45*.

In the next section we describe parameterizations of subglacial conditions that allow us to approximately match the observed seismograms. With careful choice of parameters, we are able to match the primary features of the observed spectrograms. An example is shown in Fig. 3. We match the observed variation of $f_0(t)$ during most of the period of elevated sliding, as well as seismic amplitudes and corner frequencies recorded at the seismometer BB09. We show a time slice of the spectrogram at $t = 400$ s, where $t = 0$ corresponds to the time of maximum sliding velocity, in Fig. 3c.

6 Inferences of subglacial conditions

We now place constraints on the bed shear modulus G_b, the effective pressure $\bar{\sigma}$, the patch size R, and the state evolution distance L. We hold all other parameters fixed except where explicitly mentioned (see Table 1). We first discuss the choice of frictional parameters.

6.1 Frictional parameters

The frictional parameters are chosen to have the values $a = 0.010$ and $b = 0.015$, which are typical of glacial materials (Thomason and Iverson, 2008; Rathbun et al., 2008; Iverson, 2010; Zoet et al., 2013). One effect of varying these frictional parameters is to alter a lower bound on effective pressure. This lower bound is given by the inertial stability limit of Eq. (17) and results in a direct trade-off between the frictional parameter $b - a$ and effective pressure $\bar{\sigma}$,

$$\bar{\sigma} = \frac{\eta V_s}{b - a}. \tag{18}$$

Using a $b - a$ values in the range $10^{-3} - 10^{-1}$ and the maximum observed sliding velocity gives a lower bound in the range $\bar{\sigma} \gtrsim 1$–100 kPa. For our preferred value $b - a = 0.01$, $\bar{\sigma} \gtrsim 10$ kPa. As we will discuss in Sect. 6.3, effective pressures in the upper part of this range require small patches and are not consistent with observed corner frequencies ~ 100 Hz.

6.2 Constraints on the bed shear modulus from seismic amplitudes

The shear modulus of the bed is directly constrained by combining the scaling relationships for the particle velocity amplitude (Eq. 10) and event duration (Eq. 14). The resulting scaling relation is

$$v \sim Z(G_b)\frac{D}{c_i H}\left[\frac{G_*(G_b)}{\eta(G_b)}\right]^2. \tag{19}$$

The only quantity that is not held fixed in Eq. (19) is the shear modulus of the bed G_b.

We solve Eq. (19) for B_b as a function of time for several tremor episodes. The result is plotted in Fig. 5a. The bed shear modulus is inferred to be 20.4 MPa ± 6.6 MPa for double wait time events and 19.1 MPa ± 3.9 MPa for single wait time events. Comparison with a t distribution shows that the difference in these mean values is significant at an 85 % confidence level.

We estimate that till density ρ_b lies somewhere in the range between $1700\,\mathrm{kg\,m^{-3}}$ for a till with 40 % porosity and $2200\,\mathrm{kg\,m^{-3}}$ for a till with 0 % porosity. Together, this parameter range gives a range of till shear wave speeds $c_b \equiv \sqrt{G_b/\rho_b}$ between $\sqrt{27.0/1700} \approx 127\,\mathrm{m\,s^{-1}}$ and $\sqrt{13.8/2200} \approx 80\,\mathrm{m\,s^{-1}}$, with mean value $\sqrt{15.5/2200} \approx 95\,\mathrm{m\,s^{-1}}$. This range is in rough agreement with previous studies, as we will describe in the Discussion section.

6.3 Constraints on patch size and effective pressure from fault stability and stress analysis

We now constrain conditions to lie along a 1-D subset of patch size–effective pressure space ($R - \bar{\sigma}$ space) that is consistent with inferred slip $D = V_s/f_0$. We first constrain the bed shear modulus using (Eq. 19). The resulting subset is then further refined by requiring that simulated tremor episodes also match observed corner frequencies.

We use three constraints: (1) effective pressure cannot exceed the overburden pressure, (2) fault conditions must be unstable in order to support the existence of stick-slip motion Eq. (17), and (3) slip per event D must match that inferred from V_s/f_0 Eq. (2). These three conditions are plotted in $R, \bar{\sigma}$ space in Fig. 6. The three parameter space constraints correspond to (1) a horizontal line indicating the overburden pressure, (2) a curve indicating the stability condition, and (3) a heavy line indicating the $\bar{\sigma}, R$ combinations that produce the observed slip D. The points along this line of observed slip are found by solving the minimization problem $||D(\bar{\sigma}, R) - D_{\mathrm{obs}}||$, where the slip per event at a given effective pressure and patch size $D(\bar{\sigma}, R)$ is calculated using numerical simulations.

Different $\bar{\sigma}, R$ combinations that match observed displacements are distinguished by having different corner frequencies, f_c. This is shown in the inset of Fig. 6. We recall that because we hold the bed shear modulus and slip fixed, Eq. (19) shows that seismic amplitudes do not vary for any points along the line of constant slip. Taking the corner frequency to lie in the range 50–100 Hz constrains patch size to be in the range 1.2–2.4 m. Because we cannot reliably estimate temporal variations in the corner frequency, we cannot estimate temporal variations in the tremor patch size.

Estimates of effective pressure through time are shown in Fig. 5c. Corresponding estimates of effective pressure are 26 kPa ± 6 kPa for long-wait-time events and 25 kPa ± 4 kPa for short-wait-time events. Comparison to a t distribution shows that this difference in means is significant at the 85 % level.

6.4 State evolution distance

We infer a state evolution distance L no greater than $\sim 1\,\mu$m. This claim is substantiated as follows. The stability condition Eq. (17) may be written, using the stress drop relationship Eq. (11) and the duration scaling Eq. (14), as

$$D \gtrsim V_s T + L, \tag{20}$$

where we have assumed that the stress drop scales with $(b - a)\bar{\sigma}$. Instability therefore occurs when fault slip D is greater than the critical slip distance L plus any additional slip deficit $V_s T$ that has accumulated during the slip event. The relationship Eq. (20) predicts $L \lesssim 5\,\mu$m for the extreme values of the parameters observed on the WIP.

A tighter constraint on L comes from the linear stability analysis of Dmitrieva et al. (2013). We rewrite their expression for the recurrence frequency (their supplemental Eq. 10) as

$$f_0 = \frac{1}{2\pi}\frac{V_s}{L}\sqrt{\frac{kL}{a\bar{\sigma} + \eta V_s}}. \tag{21}$$

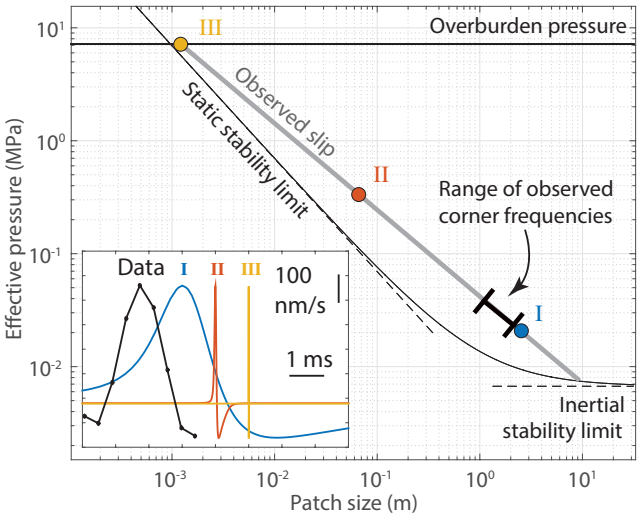

Figure 6. A diagram showing the range of patch size-effective pressure $R-\bar{\sigma}$ conditions that give rise to fault slip $D_{\mathrm{obs}} = 40\,\mu\mathrm{m\,s^{-1}}$ (thick grey line). This figure shows a snapshot of parameter space at one instance during a tremor episode; the full evolution of parameters is shown in Fig. 5. The heavy grey line shows the subset of parameter space that is also consistent with observed corner frequencies. The fault is loaded with velocity $V_{\mathrm{s}} = 0.4\,\mathrm{mm\,s^{-1}}$. The lower thin curve shows the boundary of the stability region Eq. (17). The horizontal line shows the overburden stress $\rho_{\mathrm{i}}\,g\,H$. The inset shows a representative wave pulse recorded at high rate at station GS07 on 14 December 2010 as compared to three simulated wave forms. The bed shear modulus G_{b} for the simulations is chosen from Fig. 5 to be 15 MPa. Each simulation has the same seismic amplitude and slip; they differ only corner frequency ($f_{\mathrm{c}} \approx 30$, 750, and 4000 Hz).

Solving for L, we find values of $1.4\,\mu\mathrm{m} \pm 0.4\,\mu\mathrm{m}$ (Fig. 5b). Differences between inferred state evolution distances are not significantly different for single and double wait time tremor episodes.

Micron-scale L values are on the small end of values typically inferred for geological and engineered materials (Dieterich, 2007). The critical slip distance is generally thought to be related to a material's grain size. In the case of sliding against glacial till, inferred μm L values may result from the high clay content, and therefore μm-scale grain size, of WIP till (Tulaczyk et al., 1998).

7 Variation of seismic amplitude at constant slip

The properties of long-wait-time tremor episodes are of particular interest as they may be indicative of prevailing near future conditions. Tremor episodes during double wait time events have higher amplitude ($420\,\mathrm{nm\,s^{-1}} \pm 120\,\mathrm{nm\,s^{-1}}$) than tremor episodes during single wait time events ($380\,\mathrm{nm\,s^{-1}} \pm 120\,\mathrm{nm\,s^{-1}}$). This difference in means is significant with 99 % confidence. As discussed later, we further verify this result by using a separate amplitude metric from the one discussed in Sect. 2.

The simplest explanation for this behavior is that higher amplitudes are caused by greater higher slip per event, D, as suggested by Eq. (10). This explanation, however, is not supported by the data. The mean slip per event for double and single wait time events are not significantly different at the 85 % confidence level (mean $45\,\mathrm{nm\,s^{-1}} \pm 17\,\mathrm{nm\,s^{-1}}$). We therefore consider two mechanisms for the observed seismic amplitude variation at constant slip D. First, from the analysis in Sect. 6.2, we expect that the difference in amplitudes at constant slip D may only arise from changes in the bed shear modulus. Indeed, as discussed in Sect. 6.2, higher shear modulus values are inferred for long-wait-time events. The second explanation is that the variation is due to un-modeled effects involving partitioning between seismic and aseismic slip.

Before proceeding, we first establish that the amplitude anomaly is not an artifact of the particular amplitude envelope algorithm discussed in Sect. 2. We examine a catalog of 40 tremor episodes, many of which do not have adequately clear spectral bands to perform a more detailed analysis but which are adequate for the analysis of amplitudes. We then calculate amplitude as the median of the absolute value of the seismic trace during the tremor episode. This metric provides a much lower amplitude estimate than the metric described in Sect. 2 because it includes many near-zero trace values that occur during oscillatory motion. Comparison with a t distrubtion confirms that double wait time events have higher median amplitude ($41 \pm 8\,\mathrm{nm\,s^{-1}}$) than single wait time events ($50 \pm 4\,\mathrm{nm\,s^{-1}}$) with 99.99 % certainty.

7.1 Explanation 1: actual stiffness change

The first mechanism we discuss is that the apparent variation in bed stiffness is real and involves the granular mechanics of till. Granular materials such as glacial till have elastic moduli that depend on effective pressure (Mavko et al., 2009, ch. 5.2). When a pack of grains is subjected to an increase in effective pressure, the total area of contact between the grains increases. The length scale associated with this contact area governs the strain magnitude in the grain pack and therefore sets the bulk stiffness of the grain pack. Digby (1981) describes the resulting change in elastic modulus under the assumptions of spherical particle geometry and small strains. We estimate the change in shear modulus as a function of confining pressure as described by Mavko et al. (2009). The coordination number is the number of points of contact per grain; we fix this value at $C = 9$. We also take the grain shear modulus 40 GPa and grain Poisson ratio 0.15. We choose a value for the fractional initial contact area, 0.1 %, that is taken to represent a loosely packed particle arrangement.

We calculate that a 30 % increase in the bulk shear modulus requires increasing effective pressure by a factor of 2.5. Pressure changes of this magnitude are inferred between

events (Fig. 5c), and we cannot exclude this explanation at the present time.

One limitation of this explanation is that the bed material may not be well represented as a pack of elastic spheres. WAIS subglacial till consists of an unsorted mixture of $\sim$ 30 % sand-sized particles and more than 30 % clay-sized particles by weight (Tulaczyk et al., 1998). While the sand-sized particles are well approximated as spherical; the clay-sized particles, because of their 2-D sheet structure, are not. It is not clear a priori whether the bulk stiffness of the bed material is governed by one of these phases or both. If the bulk stiffness is governed by clay phases, the basic scaling of the elastic moduli predicted by Digby (1981) may be inapplicable. Despite this shortcoming, it is not unreasonable to assume that till exhibits pressure dependence of its elastic moduli, and for this reason we do not rule out this potential explanation.

7.2 Explanation 2: aseismic slip

Another explanation is that seismic amplitudes are lower for single wait time events because more of their slip occurs aseismically. Several studies provide an observational basis for the occurrence of combined seismic and aseismic motion along isolated fault patches at ice stream beds (Anandakrishnan et al., 2001; Smith et al., 2015). This phenomenon is not necessarily captured by our idealized fault model as it requires the calculation of the spatial variation of stress and slip along the finite extent of the fault patch. Simulations that do calculate this variation, however, show that more aseismic sliding is expected to occur as a fault approaches the stability limit (Chen and Lapusta, 2009). In this near-stable limit, only a small fraction of a rate weakening patch experiences seismic slip. This type of behavior has also been invoked to explain moment-recurrence time scaling at Parkfield, CA (Nadeau and Johnson, 1998). Although our description of stress and slip on the fault does not capture this behavior, several other aspects of our description remain approximately valid for a finite fault.

When some fault motion is aseismic, the total slip during the seismic cycle consists of an aseismic part and a seismic part, $D = D_{\mathrm{A}} + D_{\mathrm{S}}$. The kinematic condition Eq. (2) must hold for the total slip, so that $D = V_{\mathrm{s}} / f_0$. Seismic amplitudes, however, are sensitive only to seismic slip. Aseismic slip therefore explains lower seismic amplitudes for single wait time events if single wait time events experience some aseismic slip.

Aseismic slip is favored for smaller magnitude events (Chen and Lapusta, 2009, their Fig. 8) as fault conditions approach stability. This could happen for a variety of reasons, including decreasing either the fault radius or effective pressure. Implications of such changes for the long term deceleration of the WIP are discussed in Sect. 8. A complete description of the potential conditions which lead to aseismic slip in the context of the subglacial environment is not currently available in the literature and further investigation in this area is certainly warranted.

8 Discussion

We have quantified the dynamics of a small fault patch at the bed of an ice stream using a spring-slider model. Motions on the fault excite seismic waves and by comparing synthetic seismograms with those that are observed we have constrained several fault zone parameters. We are able to match many of the remarkable features of the tremor episodes recorded on the Whillans Ice Plain (Fig. 3), including the variation of tremor spectral peaks with sliding velocity, seismic amplitudes, and corner frequencies.

Our simulations have constant fault zone properties throughout the tremor episode. As a result of this, our simulations do not always match the observed seismic amplitudes and recurrence frequencies during an entire tremor episode (Fig. 4). This self-imposed limitation may seem contradictory because we have just argued that the fault zone properties appear to change during a tremor episode (Fig. 5). We accept this limitation because of the possibility that 2-D or 3-D effects are involved in the observed temporal evolution during a single event.

Tremor episodes in glaciers may also be related to the motions of fluids contained within conduits (Métaxian et al., 2003; Stuart et al., 2005; Winberry et al., 2009; Gimbert et al., 2014; Lipovsky and Dunham, 2015; Bartholomaus et al., 2015). Several lines of evidence suggest that the WIP tremor episodes are not related to such a source process. The foremost reason is that on certain seismometers, tremor episodes clearly show individual slip events with clear P- and S-wave arrivals (Winberry et al., 2013). Additionally, there is a strong correlation between observed ice surface velocities and the tremor frequency, and this correlation has a clear interpretation in terms of repeating earthquakes. The relationship between surface velocities and hydraulic fracture resonance, in contrast, is not as clear. Finally, simple models of hydraulic fracture resonance (Lipovsky and Dunham, 2015) and turbulent channel flow (Gimbert et al., 2014) predict spectral signatures that are not consistent with the evenly spaced spectral peaks observed on the WIP, although complex geometrical effects may invalidate the simplifying assumptions of such models. These distinguishing criteria may be useful in analyzing several recently described data sets (Heeszel et al., 2014; Helmstetter et al., 2015a, b; Hammer et al., 2015).

Having identified a bed shear wave speed of 75–100 $\mathrm{m\,s^{-1}}$ in Sect. 6.2, we rule out the possibility that the tremor producing patch is a bedrock outcrop. We consider this inferred shear wave speed to be consistent with the presence of subglacial till (Blankenship et al., 1986). Further evidence that the fault interface consists at least partly of till is given by the relatively small estimated state evolution distance $L \sim 1\,\mu$m.

We interpret this distance to be indicative of sliding against a material with μm-scale grain size, and glacial till is the most plausible such material (Tulaczyk et al., 1998). Laboratory experiments also show that L scales with the thickness of shear zone deformation (Marone and Kilgore, 1993). Micron-scale L values therefore suggest a high degree of localization of subglacial deformation.

The WIP has long been recognized as having heterogeneous basal shear resistance (Alley, 1993). Direct borehole access to the bed has measured effective pressure in the range of -30 to 200 kPa (Kamb, 2001). Numerous ice flow model-based inversions of geodetic data have found localized regions of high basal shear stress in the vicinity of the seismometers that record the WIP tremor episodes (Joughin et al., 2004; Winberry et al., 2014c; Sergienko et al., 2014). These areas of high resistance to flow are juxtaposed against an active subglacial lake system (Siegfried et al., 2014) where basal resistance to flow is presumably negligible. Recent inversions with precise digital elevation data show that shear resistance in localized km-scale patches may be as high as 10–100 kPa. These patches exist within extensive regions that have zero shear resistance within the resolution of the inversion (O. Sergienko, personal communication, 2015). Our estimated $\sim$30 kPa effective pressure within the tremor fault zone is therefore in reasonable agreement with both borehole and geodetic stress estimates.

Our $\sim$3 kPa stress drop estimate is somewhat low but not unusual for glacier sliding earthquakes. On the Hans Glacier, Svalbard, Górski (2014) finds fault radii of 28–74 m associated with stress drops 86 Pa–1.2 kPa, respectively. On upstream sites on the Kamb and Whillans ice streams, Anandakrishnan and Alley (1994) find fault radii of 5–10 m associated with stress drops of 10–100 kPa, respectively. On the David Glacier, East Antarctica, Danesi et al. (2007) find fault radii 65–110 m associated with stress drops 100–600 kPa, respectively. The data of Górski (2014) show spectral troughs that are likely due to free surface reflections, and so their estimates of fault size should be interpreted as lower bounds (Langston, 1978). The range of stress drops given by Danesi et al. (2007) occurs because they do not account for bi-material effects and instead consider end-member elastic moduli scenarios.

Tremor events may provide insight into the mechanism of long term deceleration at the WIP. Double wait time events are becoming more common during WIP stagnation (Winberry et al., 2014c). The particular conditions that give rise to higher seismic amplitudes during double wait time events (Sect. 7) may therefore be indicative of prevailing near-future conditions of the WIP. We now discuss the markedly different predictions of each of the two mechanisms we have identified to account for this behavior.

The two mechanisms identified to account for anomalous seismic amplitudes make different predictions about fault zone stability: a stiffening bed implies a shift towards more stable conditions (by increasing k in Eq. 17), but increased seismic slip implies a shift towards less stable conditions. Independent observations from the Kamb Ice Stream seem to favor the hypothesis that during ice-stream stagnation tremor producing patches becomes more unstable to sliding. The Kamb Ice Stream has a seismicity rate that is approximately 1000 times higher than on the fast flowing, upstream part of the Whillans Ice Stream (Anandakrishnan and Bentley, 1993; Anandakrishnan and Alley, 1994, 1997). One interpretation of this observation is that as an ice stream decelerates, subglacial conditions become more unstable in the sense defined by Eq. (17). This scenario is consistent with increasing effective pressure (at constant slip, D, see Fig. 6) and is therefore consistent with a water piracy-type mechanism for ice-stream stagnation (Alley et al., 1994; Anandakrishnan and Alley, 1997).

We have conducted dynamic simulations of stick-slip motion at the bed of the Whillans Ice Plain (WIP). By comparing the simulations to data, we are able to independently infer the presence of an elastically compliant, fine-grained till layer and high pore pressures. Furthermore, seismic amplitude variations between tremor episodes may be related to long term changes occurring at the bed.

Data availability

The seismic data used in this study were downloaded from IRIS (http://www.fdsn.org/networks/detail/2C_2010). The geodetic data were obtained from Winberry et al. (2014a) and Winberry et al. (2014b).

Acknowledgements. J. Paul Winberry and Martin Pratt helped the authors work with the data that was used in their previous publications. Criticism from three anonymous reviewers significantly improved the manuscript, as did discussions with Emily Brodsky, Slawek Tulaczyk, Grace Barcheck, Susan Schwartz, Cooper Elsworth, Greg Beroza, Hilmar Gudmundson, and Yehuda Ben-Zion.

Edited by: O. Eisen

References

Aki, K. and Richards, P. G.: Quantitative Seismology, University Science Books, Sausalito, p. 23 and 110–111, 2002.

Alley, R. B.: In search of ice-stream sticky spots, J. Glaciol., 39, 447–454, 1993.

Alley, R. B., Anandakrishnan, S., Bentley, C. R., and Lord, N.: A water-piracy hypothesis for the stagnation of Ice Stream C, Antarctica, Annal. Glaciol., 20, 187–194, doi:10.3189/172756494794587032, 1994.

Ampuero, J.-P. and Dahlen, F.: Ambiguity of the moment tensor, Bull. Seis. Soc. Amer., 95, 390–400, doi:10.1785/0120040103, 2005.

Anandakrishnan, S. and Alley, R.: Ice Stream C, Antarctica, sticky spots detected by microearthquake monitoring, Ann. Glaciol., 20, 183–186, doi:10.3189/172756494794587276, 1994.

Anandakrishnan, S. and Alley, R. B.: Stagnation of Ice Stream C, West Antarctica by water piracy, Geophys. Res. Lett., 24, 265–268, doi:10.1029/96GL04016, 1997.

Anandakrishnan, S. and Bentley, C.: Micro-earthquakes beneath Ice Streams B and C, West Antarctica: observations and implications, J. Glaciol., 39, 455–462, 1993.

Anandakrishnan, S., Alley, R., Jacobel, R., and Conway, H.: The flow regime of Ice Stream C and hypotheses concerning its recent stagnation, The West Antarctic Ice Sheet: Behavior and Environment, AGU Antarctic Research Series, 77, 283–296, doi:10.1029/AR077p0283, 2001.

Bartholomaus, T. C., Amundson, J. M., Walter, J. I., O'Neel, S., West, M. E., and Larsen, C. F.: Subglacial discharge at tidewater glaciers revealed by seismic tremor, Geophys. Res. Lett., 42, 6391–6398, doi:10.1002/2015GL064590, 2015.

Bean, C. J., De Barros, L., Lokmer, I., Métaxian, J.-P., O'Brien, G., and Murphy, S.: Long-period seismicity in the shallow volcanic edifice formed from slow-rupture earthquakes, Nature Geosci., 7, 71–75, doi:10.1038/ngeo2027, 2014.

Beem, L., Tulaczyk, S., King, M., Bougamont, M., Fricker, H., and Christoffersen, P.: Variable deceleration of Whillans Ice Stream, West Antarctica, J. Geophys. Res., 119, 212–224, doi:10.1002/2013JF002958, 2014.

Ben-Zion, Y.: The response of two half spaces to point dislocations at the material interface, Geophys. J. Int., 101, 507–528, doi:10.1111/j.1365-246X.1990.tb05567.x, 1990.

Bindschadler, R. A., King, M. A., Alley, R. B., Anandakrishnan, S., and Padman, L.: Tidally controlled stick-slip discharge of a West Antarctic ice stream, Science, 301, 1087–1089, doi:10.1126/science.1087231, 2003.

Blankenship, D., Bentley, C., Rooney, S., and Alley, R. B.: Seismic measurements reveal a saturated porous layer beneath an active Antarctic ice stream, J. Geophys. Res., 322, 54–57, doi:10.1038/322054a0, 1986.

Bougamont, M., Price, S., Christoffersen, P., and Payne, A.: Dynamic patterns of ice stream flow in a 3-D higher-order ice sheet model with plastic bed and simplified hydrology, J. Geophys. Res., 116, F04018, doi:10.1029/2011JF002025, 2011.

Bougamont, M., Christoffersen, P., Price, S., Fricker, H., Tulaczyk, S., and Carter, S.: Reactivation of Kamb Ice Stream tributaries triggers century-scale reorganization of Siple Coast ice flow in West Antarctica, Geophys. Res. Lett., 42, 8471–8480, doi:10.1002/2015GL065782, 2015.

Brune, J.: Tectonic Stress and the Spectra of Seismic Shear Waves from Earthquakes, J. Geophys. Res., 75, 1970.

Chen, T. and Lapusta, N.: Scaling of small repeating earthquakes explained by interaction of seismic and aseismic slip in a rate and state fault model, J. Geophys. Res., 114, B01311, doi:10.1029/2008JB005749, 2009.

Danesi, S., Bannister, S., and Morelli, A.: Repeating earthquakes from rupture of an asperity under an Antarctic outlet glacier, Earth Planet. Sci. Lett., 253, 151–158, doi:10.1016/j.epsl.2006.10.023, 2007.

Dieterich, J.: Applications of rate-and state-dependent friction to models of fault slip and earthquake occurrence, Treat. Geophys., 4, 107–129, doi:10.1016/B978-044452748-6/00065-1, 2007.

Digby, P.: The effective elastic moduli of porous granular rocks, J. App. Mech., 48, 803–808, doi:10.1115/1.3157738, 1981.

Dmitrieva, K., Hotovec-Ellis, A. J., Prejean, S., and Dunham, E. M.: Frictional-faulting model for harmonic tremor before Redoubt Volcano eruptions, Nat. Geosci., 6, 652–656, doi:10.1038/ngeo1879, 2013.

Eshelby, J. D.: The determination of the elastic field of an ellipsoidal inclusion, and related problems, Proc. Roy. Soc. Lnd. A: Math. Phys. Eng. Sci., 241, 376–396, doi:10.1098/rspa.1957.0133, 1957.

Geubelle, P. and Breitenfeld, M.: Numerical analysis of dynamic debonding under anti-plane shear loading, Int. J. Frac., 85, 265–282, doi:10.1023/A:1007498300031, 1997.

Gimbert, F., Tsai, V. C., and Lamb, M. P.: A physical model for seismic noise generation by turbulent flow in rivers, J. Geophys. Res., 119, 2209–2238, doi:10.1002/2014JF003201, 2014.

Goldberg, D., Schoof, C., and Sergienko, O.: Stick-slip motion of an Antarctic Ice Stream: The effects of viscoelasticity, J. Geophy. Res., 119, 1564–1580, doi:10.1002/2014JF003132, 2014.

Górski, M.: Seismic Events in Glaciers, Springer, 45–70, doi:10.1007/978-3-642-31851-1, 2014.

Hammer, C., Ohrnberger, M., and Schlindwein, V.: Pattern of cryospheric seismic events observed at Ekström ice shelf, Antarctica, Geophys. Res. Lett., 3936–3943, doi:10.1002/2015GL064029, 2015.

Haran, T., Bohlander, J., Scambos, T., Painter, T., and Fahnestock, M.: MODIS Mosaic of Antarctica 2008–2009 (MOA2009) Image Map, Version 1, NSIDC – National Snow and Ice Data CenterBoulder, Colorado, USA, doi:10.7265/N5KP8037, 2014.

Heeszel, D. S., Walter, F., and Kilb, D. L.: Humming glaciers, Geology, 42, 1099–1102, doi:10.1130/G35994.1, 2014.

Helmstetter, A., Moreau, L., Nicolas, B., Comon, P., and Gay, M.: Intermediate-depth icequakes and harmonic tremor in an Alpine glacier (Glacier d'Argentière, France): Evidence for hydraulic fracturing?, J. Geophys. Res., 120, 402–416, doi:10.1002/2014JF003289, 2015a.

Helmstetter, A., Nicolas, B., Comon, P., and Gay, M.: Basal icequakes recorded beneath an Alpine glacier (Glacier d'Argentière, Mont Blanc, France): Evidence for stick-slip motion?, J. Geophys. Res., 120, 379–401, doi:10.1002/2014JF003288, 2015b.

Iverson, N. R.: Shear resistance and continuity of subglacial till: hydrology rules, J. Glaciol., 56, 1104–1114, doi:10.3189/002214311796406220, 2010.

Joughin, I. and Alley, R. B.: Stability of the West Antarctic ice sheet in a warming world, Nature Geosci., 4, 506–513, doi:10.1038/ngeo1194, 2011.

Joughin, I., MacAyeal, D. R., and Tulaczyk, S.: Basal shear stress of the Ross ice streams from control method inversions, J. Geophys. Res., 109, doi:10.1029/2003JB002960, 2004.

Kamb, B.: Basal zone of the West Antarctic ice streams and its role in lubrication of their rapid motion, The West Antarctic ice sheet: behavior and environment, 157–199, doi:10.1029/AR077p0157, 2001.

Kaneko, Y. and Shearer, P.: Seismic source spectra and estimated stress drop derived from cohesive-zone models of circular subshear rupture, Geophys. J. Int., doi:10.1002/2014JB011642, 2014.

Kyrke-Smith, T., Katz, R., and Fowler, A.: Subglacial hydrology and the formation of ice streams, Proc. Royal Soc. Lnd., 470, 20130494, doi:10.1098/rspa.2013.0494, 2014.

Kyrke-Smith, T., Katz, R., and Fowler, A.: Subglacial hydrology as a control on emergence, scale and spacing of ice streams, J. Geophys. Res., 120, 1501–1514, doi:10.1002/2015JF003505, 2015.

Langston, C. A.: Moments, corner frequencies, and the free surface, J. Geophys. Res., 83, 3422–3426, doi:10.1029/JB083iB07p03422, 1978.

Lipovsky, B. P. and Dunham, E. M.: Vibrational modes of hydraulic fractures: Inference of fracture geometry from resonant frequencies and attenuation, J. Geophys. Res., 120, 1080–1107, doi:10.1002/2014JB011286, 2015.

Lough, A. C., Barcheck, C. G., Wiens, D. A., Nyblade, A., and Anandakrishnan, S.: A previously unreported type of seismic source in the firn layer of the East Antarctic Ice Sheet, J. Geophys. Res., 120, 2237–2252, doi:10.1002/2015JF003658, 2015JF003658, 2015.

MacAyeal, D., Okal, E., Aster, R., and Bassis, J.: Seismic and hydroacoustic tremor generated by colliding icebergs, J. Geophys. Res., 113, F03011, doi:10.1029/2008JF001005, 2008.

Madariaga, R.: Dynamics of an expanding circular fault, Bull. Seis. Soc. Amer., 66, 639–666, 1976.

Marone, C. and Kilgore, B.: Scaling of the critical slip distance for seismic faulting with shear strain in fault zones, Nature, 362, 618–621, doi:10.1038/362618a0, 1993.

Mavko, G., Mukerji, T., and Dvorkin, J.: The rock physics handbook: Tools for seismic analysis of porous media, Cambridge University Press, 152–153, 2009.

Métaxian, J.-P., Araujo, S., Mora, M., and Lesage, P.: Seismicity related to the glacier of Cotopaxi Volcano, Ecuador, Geophys. Res. Lett., 30, 1483, doi:10.1029/2002GL016773, 2003.

Nadeau, R. M. and Johnson, L. R.: Seismological studies at Parkfield VI: Moment release rates and estimates of source parameters for small repeating earthquakes, Bull. Seism. Soc. Amer., 88, 790–814, 1998.

Peters, L., Anandakrishnan, S., Alley, R., and Voigt, D.: Seismic attenuation in glacial ice: A proxy for englacial temperature, J. Geophys. Res., 117, F02008, doi:10.1029/2011JF002201, 2012.

Powell, T. and Neuberg, J.: Time dependent features in tremor spectra, J. Volcan. Geotherm. Res., 128, 177–185, doi:10.1016/S0377-0273(03)00253-1, 2003.

Pratt, M. J., Winberry, J. P., Wiens, D. A., Anandakrishnan, S., and Alley, R. B.: Seismic and geodetic evidence for grounding-line control of Whillans Ice Stream stick-slip events, J. Geophys. Res., 119, 333–348, doi:10.1002/2013JF002842, 2014.

Rathbun, A. P., Marone, C., Alley, R. B., and Anandakrishnan, S.: Laboratory study of the frictional rheology of sheared till, J. Geophys. Res., 113, F02020, doi:10.1029/2007JF000815, 2008.

Rice, J. R., Lapusta, N., and Ranjith, K.: Rate and state dependent friction and the stability of sliding between elastically deformable solids, Journal of the Mechanics and Physics of Solids, 49, 1865–1898, doi:10.1016/S0022-5096(01)00042-4, 2001.

Rignot, E., Mouginot, J., and Scheuchl, B.: Ice flow of the Antarctic ice sheet, Science, 333, 1427–1430, doi:10.1126/science.1208336, 2011.

Robel, A. A., DeGiuli, E., Schoof, C., and Tziperman, E.: Dynamics of ice stream temporal variability: Modes, scales, and hysteresis, J. Geophys. Res., 118, 925–936, doi:10.1002/jgrf.20072, 2013.

Scambos, T., Haran, T., Fahnestock, M., Painter, T., and Bohlander, J.: MODIS-based Mosaic of Antarctica (MOA) Data Sets: Continent-wide Surface Morphology and Snow Grain Size, Remote Sens. Environ., 111, 242–257, doi:10.1016/j.rse.2006.12.020, 2007.

Sergienko, O., Creyts, T., and Hindmarsh, R.: Similarity of organized patterns in driving and basal stresses of Antarctic and Greenland ice sheets beneath extensive areas of basal sliding, Geophys. Res. Lett., 41, 3925–3932, doi:10.1002/2014GL059976, 2014.

Sergienko, O. V., MacAyeal, D. R., and Bindschadler, R. A.: Stick–slip behavior of ice streams: modeling investigations, Annal. Glaciol., 50, 87–94, doi:10.3189/172756409789624274, 2009.

Siegfried, M. R., Fricker, H. A., Roberts, M., Scambos, T. A., and Tulaczyk, S.: A decade of West Antarctic subglacial lake interactions from combined ICESat and CryoSat-2 altimetry, Geophys. Res. Lett., 41, 891–898, doi:10.1002/2013GL058616, 2014.

Smith, E., Smith, A., White, R., Brisbourne, A., and Pritchard, H.: Mapping the Ice-Bed Interface Characteristics of Rutford Ice Stream, West Antarctica, Using Microseismicity, J. Geophys. Res., 120, 1881–1894, doi:10.1002/2015JF003587, 2015.

Stuart, G., Murray, T., Brisbourne, A., Styles, P., and Toon, S.: Seismic emissions from a surging glacier: Bakaninbreen, Svalbard, Ann. Glaciol., 42, 151–157, doi:10.3189/172756405781812538, 2005.

Thomason, J. F. and Iverson, N. R.: A laboratory study of particle ploughing and pore-pressure feedback: a velocity-weakening mechanism for soft glacier beds, J. Glaciol., 54, 169–181, doi:10.3189/002214308784409008, 2008.

Trigg, G.: Mathematical Tools for Physicists, Wiley, 2006.

Tulaczyk, S., Kamb, B., Scherer, R., and Engelhardt, H.: Sedimentary processes at the base of a West Antarctic ice stream: constraints from textural and compositional properties of subglacial debris, J. Sed. Res., 68, 487–496, 1998.

Tulaczyk, S., Kamb, W. B., and Engelhardt, H. F.: Basal mechanics of ice stream B, West Antarctica: 1. Till mechanics, J. Geophy. Res., 105, 463–481, doi:10.1029/1999JB900329, 2000.

Walter, J., Svetlizky, I., Fineberg, J., Brodsky, E., Tulaczyk, S., Barcheck, C., and Carter, S.: Rupture speed dependence on initial stress profiles: Insights from glacier and laboratory stick-slip, Earth Planet. Sci. Lett., 411, doi:10.1016/j.epsl.2014.11.025, 2015.

Walter, J. I., Brodsky, E. E., Tulaczyk, S., Schwartz, S. Y., and Pettersson, R.: Transient slip events from near-field seismic and geodetic data on a glacier fault, Whillans Ice Plain, West Antarctica, J. Geophys. Res., 116, F01021, doi:10.1029/2010JF001754, 2011.

Whillans, I., Bolzan, J., and Shabtaie, S.: Velocity of ice streams B and C, Antarctica, J. Geophys. Res., 92, 8895–8902, 1987.

Wiens, D. A., Anandakrishnan, S., Winberry, J. P., and King, M. A.: Simultaneous teleseismic and geodetic observations of the stick–slip motion of an Antarctic ice stream, Nature, 453, 770–774, doi:10.1038/nature06990, 2008.

Willis, J.: The penny-shaped crack on an interface, Quart. J. Mech. Appl. Math., 25, 367–385, doi:10.1093/qjmam/25.3.367, 1972.

Winberry, J., Anandakrishnan, S., and Alley, R.: Seismic observations of transient subglacial water-flow beneath MacAyeal Ice Stream, West Antarctica, Geophys. Res. Lett., 36, 11502, doi:10.1029/2009GL037730, 2009.

Winberry, J., Anandakrishnan, S., Wiens, D., and Alley, R.: Nucleation and seismic tremor associated with the glacial earth-

quakes of Whillans Ice Stream, Antarctica, Geophys. Res. Lett., 40, 312–315, doi:10.1002/grl.50130, 2013.

Winberry, J., Anandakrishnan, S., and Wiens, D.: Whillans Stick-slip 2010, UNAVCO, doi:10.7283/T5XG9PFJ, GPS Data Set, 2014a.

Winberry, J., Anandakrishnan, S., and Wiens, D.: Whillans Stick-slip 2011, UNAVCO, doi:10.7283/T5SQ8XPC, GPS Data Set, 2014b.

Winberry, J. P., Anandakrishnan, S., Alley, R. B., Wiens, D. A., and Pratt, M. J.: Tidal pacing, skipped slips and the slowdown of Whillans Ice Stream, Antarctica, J. Glaciol., 60, 795–807, doi:10.3189/2014JoG14J038, 2014c.

Wittlinger, G. and Farra, V.: Observation of low shear wave velocity at the base of the polar ice sheets: evidence for enhanced anisotropy, Geophys. J. Int., 190, 391–405, doi:10.1111/j.1365-246X.2012.05474.x, 2012.

Zoet, L., Carpenter, B., Scuderi, M., Alley, R., Anandakrishnan, S., Marone, C., and Jackson, M.: The effects of entrained debris on the basal sliding stability of a glacier, J. Geophys. Res., 118, 656–666, doi:10.1002/jgrf.20052, 2013.